J Comput Electron (2011) 10:300–313
DOI 10.1007/s10825-011-0366-7

Component mode synthesis approaches for quantum mechanical electrostatic analysis of nanoscale devices

H. Li · G. Li

Published online: 17 June 2011

Abstract In this paper, two component mode synthesis (CMS) approaches, namely, the fixed interface CMS approach and the free interface CMS approach, are presented and compared for an efficient solution of 2-D Schrödinger-Poisson equations for quantum-mechanical electrostatic analyses of nanostructures and devices with arbitrary geometries. In the CMS approaches, a nanostructure is divided into a set of substructures or components and the eigenvalues (energy levels) and eigenvectors (wave functions) are computed first for all the substructures. The computed wave functions are then combined with constraint or attachment modes to construct a transformation matrix. By using the transformation matrix, a reduced-order system of the Schrödinger equation is obtained for the entire nanostructure. The global energy levels and wave functions can be obtained with the reduced-order system. Through an iteration procedure between the Schrödinger and Poisson equations, a self-consistent solution for charge concentration and potential profile can be obtained. Numerical calculations show that both CMS approaches can largely reduce the computational cost. The free interface CMS approach can provide significantly more accurate results than the fixed interface CMS approach with the same number of retained wave functions in each component. However, the fixed interface CMS approach is more efficient than the free interface CMS approach when large degrees of freedom are included in the simulation.

Keywords Quantum mechanical electrostatic analysis · Component mode synthesis · Schrodinger-Poisson · Nano device electrostatics

H. Li · G. Li (✉)
Department of Mechanical Engineering, Clemson University, Clemson, SC 29634, USA
e-mail: gli@clemson.edu

1 Introduction

As the dimensions of commonly used semiconductor devices have shrunk into nanometer regime [1–4], it is recognized that the influence of quantum effects on their electrical properties cannot be ignored [5–8]. Various computational models and approaches [9–18] have been developed to analyze these properties including the quantum effects in nanostructures and devices in the past few decades. Among these computational models, the Schrödinger-Poisson model [14–18] has been widely adopted for quantum mechanical electrostatic analysis of nanostructures and devices such as quantum wires, MOSFETs and nanoelectromechanical systems (NEMS). The numerical results allow for evaluations of the electrical properties such as charge concentration and potential profile in these structures. The emerge of MOSFETs with multiple gates, such as Trigates, FinFETs and Pi-gates, offers a superior electrostatic control of devices by the gates, which can be therefore used to reduce the short channel effects within those devices. A full 2-D electrostatic analysis [19, 20] in the cross-section perpendicular to the transport direction in those nanodevices can be used to better understand the scalability of devices, moreover, many simulations and studies [21–26] focusing on the corner effects, the properties of inversion layers, current oscillations due to the applied gate voltages, and threshold voltages of multiple-gate MOSFETs have been carried out by applying the Schrödinger-Poisson model. This model is also used in the quantum simulation of silicon nanowire transistors by NEGF recently [27], an application of this model to obtain the electron sub-bands and wave functions in the devices is necessary to analyze transport characteristics of the transistors. The Schrödinger-Poisson model is attractive due to its simplicity and straightforward implementation by using standard finite difference or finite element methods. How-

ever, as it is required to solve a generalized eigenvalue problem generated from the discretization of the Schrödinger equation, the computational cost of the analysis increases quickly when the system's degrees of freedom (DOFs) increase. It is reported that solving Schrödinger equation to obtain the electron sub-bands and wave functions within the cross-section perpendicular to the transport direction consumes most of the CPU time in the whole simulation [27, 28]. For this reason, techniques that enable an efficient solution of discretized Schrödinger equation in multidimensional domains are desirable.

In this work, we seek to accelerate the numerical solution of the Schrödinger equation by using component mode synthesis (CMS) approaches [29–40]. As a model order reduction method, the CMS was originally developed for dynamic analysis of large mechanical systems. In the mechanical analysis using CMS approaches, a large structure is discretized into substructures or components. The component vibrational modes are computed for each substructure. Only a small set of component modes are retained to construct a set of Ritz basis vectors [37]. The basis vectors are used to approximate the displacement of the substructure. The approximations of the substructures are then assembled to obtain a global approximation of the entire structure's displacement. In this paper, the CMS approaches are extended in the quantum mechanical electrostatic analysis where a set of basis vectors are constructed to approximate the wave functions in each component. The global energy levels and wave functions are then recovered by the synthesis of these component wave functions. Different from mechanical analysis where only a few vibrational modes are sufficient to model the dynamic response, in some cases, it is necessary to calculate many energy levels and wave functions in order to compute the charge concentrations accurately. In our analysis, it is observed that the construction of the basis vectors plays a critical role in the accuracy of the final results. We investigate the performance of two CMS approaches with different ways of constructing basis vectors, namely, the fixed interface CMS approach and the free interface CMS approach. The fixed interface CMS approach computes fixed interface wave functions and constraint modes [38] to form the basis vectors while the free interface CMS approach employs a set of free interface wave functions, attachment modes and rigid body modes [37, 38] to form the basis vectors. The two CMS approaches are applied to compute the charge concentrations and potential profiles of several 2-D semiconductor devices including quantum wire, and multiple-gate MOSFETs. It is shown that both approaches greatly reduce the computational cost while the free interface CMS approach gives significantly more accurate results of the energy levels and wave functions. However, when large degrees of freedom are included in the simulation, the fixed interface CMS approach is more efficient than the free interface CMS approach.

The rest of the paper is organized as follows. Section 2 describes the self-consistent numerical solution of Schrödinger-Poisson equations, the CMS approaches for solving the Schrödinger equation are presented in Sect. 3, numerical examples are presented in Sect. 4, and Sect. 5 presents the conclusions.

2 Quantum mechanical electrostatic analysis

2.1 Governing equations of the Schrödinger-Poisson model

In the 2-D quantum mechanical electrostatic analysis using Schrödinger-Poisson model, the two dimensional effective mass Schrödinger equation is given by [19]

$$H\psi_n = -\frac{\hbar^2}{2m_x^*}\frac{\partial^2\psi_n}{\partial x^2} - \frac{\hbar^2}{2m_y^*}\frac{\partial^2\psi_n}{\partial y^2} + U(V_h, e\phi)\psi_n = E_n\psi_n \tag{1}$$

where H is the Hamiltonian, U is the potential energy, m_x^* and m_y^* are the effective masses of electrons or holes in x- and y-directions, respectively, ψ_n is the wave function corresponding to the energy level E_n, and V_h is the pseudo-potential energy due to the band offset at the heterostructure interface. By solving the Schrödinger equation, (1), the energy levels E_n and the corresponding wave functions ψ_n can be obtained for electrons and holes.

The Schrödinger equation is coupled with the Poisson equation through the quantum electron and hole concentrations,

$$n(\phi) = \frac{N_{nd}}{\pi}\left(\frac{2m_{nz}^* k_B T}{\hbar^2}\right)^{1/2} \times \sum_{n=1}^{\infty}\psi_n(\phi)^2 \Im_{-1/2}\left(\frac{E_F - E_n(\phi)}{k_B T}\right) \tag{2}$$

$$p(\phi) = \frac{N_{pd}}{\pi}\left(\frac{2m_{pz}^* k_B T}{\hbar^2}\right)^{1/2} \times \sum_{n=1}^{\infty}\psi_n(\phi)^2 \Im_{-1/2}\left(\frac{E_n(\phi) - E_F}{k_B T}\right) \tag{3}$$

where N_{nd} and N_{pd} are the band degeneracy of electrons and holes, respectively, m_{nz}^* and m_{pz}^* are the effective masses of electrons and holes in z-direction, respectively, E_F is the Fermi energy, and $\Im_{-1/2}$ is the complete Fermi-Dirac integral of order $-1/2$. The electron and hole concentrations can then be substituted into Poisson equation to obtain potential profile in semiconductor devices. The Poisson equation is expressed as

$$\nabla\cdot[\epsilon\nabla\phi] = -q\left[-n[\phi] + p[\phi] + N_D^+[\phi] - N_A^-[\phi]\right] \tag{4}$$

where ϵ is the dielectric constant, q is the unit electric charge, n and p are electron and hole concentrations given

in (2), (3), N_D^+ and N_A^- are ionized donor and acceptor concentrations. To obtain a self-consistent solution of the coupled Schrödinger-Poisson equations, one needs to iterate between the Schrödinger and Poisson equations. By solving the Schrödinger equation with a trial potential energy U, the eigenvalues and eigenvectors are obtained. The electron and hole concentrations are then computed based on these eigen-pairs. Substituting the computed electron and hole concentrations into the Poisson equation, a new potential profile ϕ can be calculated. The new potential profile is then used to solve the Schrödinger equation again to obtain new eigenvalues E_n and corresponding eigenvectors. By following this iteration procedure, with a number of iterations, a final solution of charge concentration and potential profile satisfying given convergence criteria can be obtained. While this relaxation scheme is straightforward, it has been shown that its convergence property is poor [18–20]. In this work, instead of solving the linear Poisson equation shown in (4), we employ a predictor-corrector approach proposed by Trellakis et al. [19] to obtain improved convergence. In the predictor-corrector approach, assuming an electron dominant case, $n[\phi]$ in the Poisson equation is replaced by a modified quantum electron concentration $\tilde{n}[\phi]$,

$$\nabla \cdot [\epsilon \nabla \phi] = -q\big[-\tilde{n}[\phi] + p[\phi] + N_D^+[\phi] - N_A^-[\phi]\big] \tag{5}$$

where

$$\tilde{n}(\phi) = \frac{N_{nd}}{\pi}\left(\frac{2m_{nz}^* k_B T}{\hbar^2}\right)^{1/2} \times \sum_{n=1}^{\infty} (\psi_n^k)^2 \Im_{-1/2}\left(\frac{E_F - E_n^k + q(\phi - \phi^k)}{k_B T}\right) \tag{6}$$

The superscript k denotes the quantities obtained from the previous Schrödinger-Poisson iteration. Note that the Poisson equation becomes nonlinear due to the modified quantum electron concentration.

2.2 Finite element solution of coupled Schrödinger and Poisson equations

The governing equations given in (1), (5) are solved by using the Finite Element Method (FEM). With the Dirichlet boundary condition $\psi_n = 0$ for the wave functions along the boundaries of the simulation domain Ω, the governing PDE of the Schrödinger equation can be converted to its weak form by using Galerkin weighted residual method. Multiplying both sides of (1) by the variation of the wave functions, $\delta\psi_n$, and integrating the product over the 2-D domain, we obtain

$$\frac{\hbar^2}{2}\int_\Omega (\nabla\psi_n)^T \mathbf{M}^* \nabla\delta\psi_n d\Omega + \int_\Omega U(V_h, e\phi)\psi_n \delta\psi_n d\Omega - \int_\Omega E_n \psi_n \delta\psi_n d\Omega = 0 \tag{7}$$

where $\mathbf{M}^*$ is a 2×2 diagonal matrix with $1/m_x^*$ and $1/m_y^*$ as its diagonal elements. Equation (7) is discretized by meshing the whole domain into a set of elements. The unknown wave functions ψ_n can be expanded as

$$\psi_n = \sum_{i=1}^{N_s} N_i(x, y)\psi_i \tag{8}$$

where N_s is the number of nodes in an element, ψ_i is the wave function on node i and $N_i(x, y)$ are the 2-D shape functions. Substituting (8) into (7), the Schrödinger equation can be rewritten in matrix form

$$(\mathbf{\Phi} - E\mathbf{M})\boldsymbol{\psi} = 0 \tag{9}$$

where $\mathbf{\Phi}$ is a symmetric matrix, $\mathbf{M}$ is a positive definite symmetric matrix. By solving the generalized eigenvalue problem, (9), a set of energy levels E_n and wave functions ψ_n can be obtained. Substituting the eigen-pairs into (2) and (3), the electron and hole concentrations can be computed.

The Poisson equation is solved over the same domain Ω to obtain the potential profile. By using the Galerkin weighted residual method, the weak form of the Poisson equation is obtained as

$$\int_\Gamma \epsilon \frac{\partial\phi}{\partial n}\delta\phi d\Gamma - \int_\Omega \epsilon\nabla\phi\cdot\nabla\delta\phi d\Omega = \int_\Omega -q\big[-\tilde{n}[\phi] + p[\phi] + N_D^+[\phi] - N_A^-[\phi]\big]\delta\phi d\Omega \tag{10}$$

where $\delta\phi$ is the variation of the potential, Γ denotes the domain boundary, and n is the boundary unit outward normal vector. The weak form of the nonlinear Poisson's equation, (10), is solved by using the Newton-Raphson method. The system equations can be written as

$$\mathbf{J}\Delta\boldsymbol{\phi} = -\mathbf{R} \tag{11}$$

where $\mathbf{J}$ is the Jacobian matrix, $\Delta\boldsymbol{\phi}$ is the potential increment and $\mathbf{R}$ is the residual vector. Note that in the calculation of the Jacobian matrix, the derivative of the modified quantum electron concentration with respect to ϕ is computed by [19]

$$\frac{\partial\tilde{n_q}[\phi]}{\partial\phi} = \frac{qN_{nd}}{\pi\hbar}\left(\frac{2m_{nz}^*}{k_B T}\right)^{1/2} \times \sum_{n=1}^{\infty}(\psi_n^k)^2 \Im_{-3/2}\left(\frac{E_F - E_n^k + q(\phi-\phi^k)}{k_B T}\right) \tag{12}$$

3 CMS approaches for solving the Schrödinger equation

The general CMS framework is comprised of four basic steps: the division of the domain Ω into a set of components, the definition of component basis vectors, the coupling of the components to form a reduced-order global system, and the recovery of the global wave functions. Figure 1 shows an example of domain decomposition in the CMS approaches. A meshed domain is discretized into a set of components.

When a component boundary edge is on the global domain boundary with a homogeneous Dirichlet boundary condition, the component is referred to as a restrained component. Otherwise it is referred to as an unrestrained component. A component boundary edge that is shared by another component is referred to as an interface edge. After the domain decomposition, depending on the methods of defining the component basis vectors, there are two major variants of the CMS: the fixed-interface CMS approach [29] and the free interface CMS approach [34]. In this section, we describe the procedures of solving the effective mass Schrödinger equation (1) by using each of the approaches.

3.1 Fixed-interface CMS approach

For each component obtained from the domain decomposition as shown in Fig. 1, the eigenvalue problem can be denoted as

$$\left(\mathbf{\Phi}^j - E^j \mathbf{M}^j\right)\boldsymbol{\psi}^j = 0 \quad j = 1, 2, \ldots, m \tag{13}$$

where j denotes the component number, m is the total number of components. In an electrostatic analysis, the wave function ψ is zero on the domain boundary. Therefore, the wave function degrees of freedom (DOFs) on the global boundary can be discarded. In fixed interface CMS approach, the wave function vector $\boldsymbol{\psi}^j$ is partitioned into two parts which are referred to as the *attachment* part and *interior* part. The attachment part contains the wave function DOFs at nodes on interface edges which are shared by different components, and interior part contains the DOFs associated with the interior nodes of the component. The attachment and interior parts of $\boldsymbol{\psi}^j$ are denoted by subscripts a and i, respectively. With respect to the attachment and interior DOFs, (13) can be partitioned as

$$\left(\begin{bmatrix} \mathbf{\Phi}^j_{ii} & \mathbf{\Phi}^j_{ia} \\ \mathbf{\Phi}^j_{ai} & \mathbf{\Phi}^j_{aa} \end{bmatrix} - E^j \begin{bmatrix} \mathbf{M}^j_{ii} & \mathbf{M}^j_{ia} \\ \mathbf{M}^j_{ai} & \mathbf{M}^j_{aa} \end{bmatrix}\right) \begin{Bmatrix} \boldsymbol{\psi}^j_i \\ \boldsymbol{\psi}^j_a \end{Bmatrix} = \begin{Bmatrix} \mathbf{0} \\ \mathbf{0} \end{Bmatrix} \tag{14}$$

In the fixed interface CMS approach, the attachment DOFs are set to be fixed, i.e., $\boldsymbol{\psi}^j_a = 0$, we obtain from (14)

$$\left(\mathbf{\Phi}^j_{ii} - E^j \mathbf{M}^j_{ii}\right)\boldsymbol{\psi}^j_i = \mathbf{0} \tag{15}$$

The eigen-pairs $(E^j, \boldsymbol{\psi}^j_i)$ can be thus computed from (15) for a component j. In CMS, a small set of $\boldsymbol{\psi}^j_i$ corresponding to a few lowest energy levels obtained from (15) are retained and assembled column-wisely into the component modal matrix $\bar{\mathbf{D}}^j_i$, i.e.,

$$\bar{\mathbf{D}}^j_i = \left[\boldsymbol{\psi}^j_{i1}\ \boldsymbol{\psi}^j_{i2}\ \boldsymbol{\psi}^j_{i3}\ \cdots\ \boldsymbol{\psi}^j_{ik}\right] \tag{16}$$

where $k \ll$ *interior DOFs* is the number of $\boldsymbol{\psi}^j_i$ which are retained in $\bar{\mathbf{D}}^j_i$. Next, a constraint modal matrix is obtained by applying $E^j = 0$ in the component and enforcing a unit wave function on the attachment DOFs in (14), i.e.,

$$\begin{bmatrix} \mathbf{\Phi}^j_{ii} & \mathbf{\Phi}^j_{ia} \\ \mathbf{\Phi}^j_{ai} & \mathbf{\Phi}^j_{aa} \end{bmatrix} \begin{Bmatrix} \mathbf{X}^j_i \\ \mathbf{I}_a \end{Bmatrix} = \begin{Bmatrix} \mathbf{0} \\ \mathbf{R}^j_a \end{Bmatrix} \tag{17}$$

where each column of the identity matrix $\mathbf{I}_a$ is used to enforce a unit magnitude of the wave function on one attachment DOF with the wave functions on other attachment DOFs fixed to zeros, $\mathbf{R}^j_a$ is the resultant boundary reaction at the attachment DOFs. The expression of the constraint modal matrix $\mathbf{X}^j_i$ for the interior DOFs can be obtained from (17) explicitly as

$$\mathbf{X}^j_i = -(\mathbf{\Phi}^j_{ii})^{-1}\mathbf{\Phi}^j_{ia} \tag{18}$$

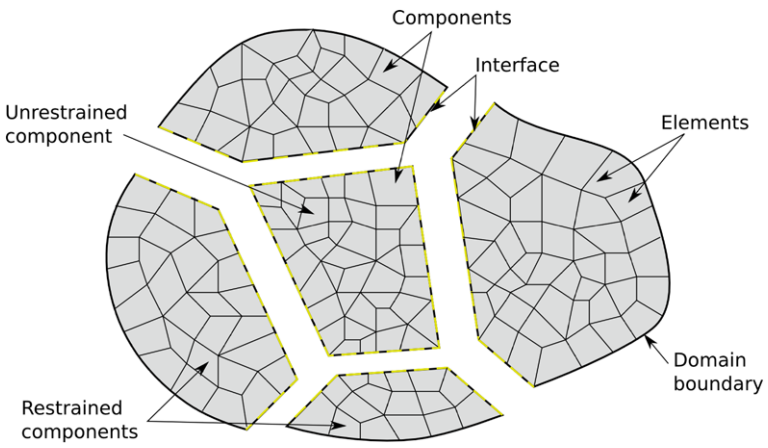

Fig. 1 Domain decomposition in CMS approaches

Having obtained $\bar{\mathbf{D}}_i^j$ and $\mathbf{X}_i^j$, the component wave functions are then approximated by

$$\boldsymbol{\psi}^j = \begin{Bmatrix} \boldsymbol{\psi}_i^j \\ \boldsymbol{\psi}_a^j \end{Bmatrix}_{n\times 1} = \begin{bmatrix} \bar{\mathbf{D}}_i^j & \mathbf{X}_i^j \\ \mathbf{0}_a & \mathbf{I}_a \end{bmatrix}_{n\times r} \begin{Bmatrix} \mathbf{z}_i^j \\ \boldsymbol{\psi}_a^j \end{Bmatrix}_{r\times 1} \tag{19}$$

where n is the total component DOFs, $r = k + a$ is the sum of retained component $\boldsymbol{\psi}_i^j$ and the attachment DOFs, $\mathbf{I}_a$ and $\mathbf{0}_a$ are identity and zero matrix associated with attachment DOFs, respectively, the vector $\begin{Bmatrix} \mathbf{z}_i^j \\ \boldsymbol{\psi}_a^j \end{Bmatrix}$ is a generalized coordinate vector. Equation (19) can be rewritten in short form as,

$$\boldsymbol{\psi}^j = \mathbf{T}^j \mathbf{z}^j \tag{20}$$

where $\mathbf{T}^j$ is referred to as the transformation matrix of component j. Equation (20) shows that the wave functions of a component can be approximated as a linear combination of the column vectors of $\mathbf{T}^j$ with elements of the vector $\mathbf{z}^j$ acting as the coefficients, i.e., the column vectors of $\mathbf{T}^j$ are the basis vectors of component j. Note that, since $k \ll \textit{interior DOFs}, r \ll n$. This property enables CMS to reduce the computational cost of calculating both component and global wave functions, and, on the other side, introduces an approximation error. Substituting (20) into (13), we obtain

$$\left(\boldsymbol{\Phi}^j - E^j \mathbf{M}^j\right)\mathbf{T}^j \mathbf{z}^j = \mathbf{0} \tag{21}$$

Multiplying the transpose of $\mathbf{T}^j$ to both sides of (21) gives

$$\left(\mathbf{T}^j\right)^T \left(\boldsymbol{\Phi}^j - E^j \mathbf{M}^j\right)\mathbf{T}^j \mathbf{z}^j = \mathbf{0} \tag{22}$$

Equation (22) can be rewritten in the short form as

$$(\bar{\boldsymbol{\Phi}}^j - E^j \bar{\mathbf{M}}^j)\mathbf{z}^j = \mathbf{0} \tag{23}$$

where

$$\bar{\boldsymbol{\Phi}}^j = (T^j)^T \boldsymbol{\Phi}^j \mathbf{T}^j \tag{24}$$

and

$$\bar{\mathbf{M}}^j = (\mathbf{T}^j)^T \mathbf{M}^j \mathbf{T}^j \tag{25}$$

are the reduced matrices for the component. Following the standard finite element assembly procedure, one can assemble (23) of the connected components into a global modal system, i.e.,

$$(\hat{\boldsymbol{\Phi}} - E\hat{\mathbf{M}})\hat{\mathbf{z}} = \mathbf{0} \tag{26}$$

where

$$\hat{\boldsymbol{\Phi}} = \textit{assemble}\left(\bar{\boldsymbol{\Phi}}^1, \bar{\boldsymbol{\Phi}}^2, \bar{\boldsymbol{\Phi}}^3, \ldots, \bar{\boldsymbol{\Phi}}^m\right) \tag{27}$$

$$\hat{\mathbf{M}} = \textit{assemble}\left(\bar{\mathbf{M}}^1, \bar{\mathbf{M}}^2, \bar{\mathbf{M}}^3, \ldots, \bar{\mathbf{M}}^m\right) \tag{28}$$

By solving (26), the eigenvalues and the corresponding eigenvectors $\hat{\mathbf{z}}$ of the entire system can be obtained. The global wave functions $\boldsymbol{\psi}$ can be computed by

$$\boldsymbol{\psi} = \hat{\mathbf{T}}\hat{\mathbf{z}} \tag{29}$$

where

$$\hat{\mathbf{T}} = \textit{assemble}\left(\mathbf{T}^1, \mathbf{T}^2, \mathbf{T}^3, \ldots, \mathbf{T}^m\right) \tag{30}$$

Note that, since the number of the component basis vectors is much less than the component DOFs, the dimension of (26) is much less than the total DOFs of the system. Consequently, the computational cost of solving the Schrödinger equation is largely reduced. The fixed interface CMS approach has several advantages including: (1) its simple procedure for computing the basis vectors in the transformation matrix, (2) the straightforward implementation of coupling the components to form the global modal system, and (3) its high accuracy in computing the low eigenvalues and their corresponding eigenvectors. For these reasons, the fixed interface CMS approach has been widely adopted for large scale structural dynamic problems.

3.2 Free-interface CMS approach

In the free interface CMS approach, the eigenvalue problem for the components is also given by (13). However, while the component basis vectors are obtained by fixing the wave functions at the component interfaces in the fixed interface CMS approach, the free interface CMS makes use of a set of pre-selected free interface wave functions along with a set of attachment modes and rigid body modes [37, 38]. In solving (13), the free interface CMS does not set the component wave functions on the component interfaces to be zeros. Instead, the wave functions on the interfaces are "free". Therefore, (13) is solved directly without being converted to (15). In addition, the free interface CMS approach treats the restrained and unrestrained components separately.

3.2.1 Restrained components

For the restrained components as shown in Fig. 1, the free interface CMS approximation of the component wave functions is in the form of

$$\begin{aligned} \boldsymbol{\psi}^j &= \begin{Bmatrix} \boldsymbol{\psi}_i^j \\ \boldsymbol{\psi}_a^j \end{Bmatrix}_{n\times 1} = \begin{bmatrix} \bar{\mathbf{D}}_i^j & \mathbf{X}_i^j \\ \bar{\mathbf{D}}_a^j & \mathbf{X}_a^j \end{bmatrix}_{n\times r} \begin{Bmatrix} \mathbf{p}_i^j \\ \mathbf{p}_a^j \end{Bmatrix}_{r\times 1} \\ &= \left[\bar{\mathbf{D}}^j \mathbf{X}^j\right]_{n\times r} \left(\mathbf{p}^j\right)_{r\times 1} \end{aligned} \tag{31}$$

where $\bar{\mathbf{D}}^j$ is the matrix of retained free interface component wave functions, $\mathbf{X}^j$ is the attachment modal matrix, and $\mathbf{p}^j$ is the vector of generalized coordinates. Once again, $\bar{\mathbf{D}}^j$, $\mathbf{X}^j$ and $\mathbf{p}^j$ are partitioned into the interior (subscript i) and attachment (subscript a) parts for each component. The set

of basis vectors included in $\bar{\mathbf{D}}^j$ represents the intrinsic wave functions of the component, while the attachment modal matrix $\mathbf{X}^j$ contains the wave functions excited by the adjacent components. It has been shown that, without $\mathbf{X}^j$, the component basis set is incomplete, which will lead to unacceptable results [37]. $\bar{\mathbf{D}}^j$ is assembled column-wisely by a small set of $\boldsymbol{\psi}^j$ corresponding to the lowest energy levels obtained from (13), i.e.,

$$\bar{\mathbf{D}}^j = \left[\boldsymbol{\psi}^j_{i1}\ \boldsymbol{\psi}^j_{i2}\ \boldsymbol{\psi}^j_{i3}\ \cdots\ \boldsymbol{\psi}^j_{ik}\right]_{n\times k} \tag{32}$$

where k denotes the number of the component wave functions kept in $\bar{\mathbf{D}}^j$. Note that, in the solution of (13), the wave functions $\boldsymbol{\psi}^j$ should be mass normalized. This condition is assumed throughout the paper. Like (20), (31) can be rewritten in a short form as

$$\boldsymbol{\psi}^j = \mathbf{T}^j \mathbf{p}^j \tag{33}$$

where $\mathbf{T}^j$ is the transformation matrix containing all the component basis vectors. We apply an analogy to structural dynamics analysis, the attachment modal matrix $\mathbf{X}^j$ for restrained components are obtained by applying unit "forces" on the interface coordinates and setting $E^j = 0$ for (14), i.e.,

$$\begin{bmatrix} \boldsymbol{\Phi}^j_{ii} & \boldsymbol{\Phi}^j_{ia} \\ \boldsymbol{\Phi}^j_{ai} & \boldsymbol{\Phi}^j_{aa} \end{bmatrix}_{n\times n} \begin{bmatrix} \bar{\boldsymbol{\psi}}^j_i \\ \bar{\boldsymbol{\psi}}^j_a \end{bmatrix}_{n\times a} = \begin{bmatrix} \mathbf{0}^j_i \\ \mathbf{I}^j_a \end{bmatrix}_{n\times a} \tag{34}$$

where $\begin{bmatrix} \bar{\boldsymbol{\psi}}^j_i \\ \bar{\boldsymbol{\psi}}^j_a \end{bmatrix}$ represents the wave function response to the right hand excitation. The portion of the wave function response contributed by the retained component wave functions (i.e. the k basis vectors retained in $\bar{\mathbf{D}}^j$ as shown in (32)) should be deducted to ensure the obtained attachment modes to be Hamiltonian orthogonal to the retained component wave functions [37]. The attachment modal matrix can then be obtained as

$$\mathbf{X}^j = \begin{bmatrix} \bar{\boldsymbol{\psi}}^j_i \\ \bar{\boldsymbol{\psi}}^j_a \end{bmatrix}_{n\times a} - (\bar{\mathbf{D}}^j)_{n\times k} (\mathbf{E}^j)^{-1}_{k\times k} (\bar{\mathbf{D}}^j)^T_{k\times n} \begin{bmatrix} \mathbf{0}^j_i \\ \mathbf{I}^j_a \end{bmatrix}_{n\times a} \tag{35}$$

where the second term on the right hand side is the wave function response contributed by $\bar{\mathbf{D}}^j$.

3.2.2 Unrestrained components

For the unrestrained components (those with rigid body modes), the free interface CMS approximation has the same form of (31)

$$\begin{aligned} \boldsymbol{\psi}^j &= \begin{Bmatrix} \boldsymbol{\psi}^j_i \\ \boldsymbol{\psi}^j_a \end{Bmatrix}_{n\times 1} = \begin{bmatrix} \bar{\mathbf{D}}^j_i & \mathbf{X}^j_i \\ \bar{\mathbf{D}}^j_a & \mathbf{X}^j_a \end{bmatrix}_{n\times r} \begin{Bmatrix} \mathbf{p}^j_i \\ \mathbf{p}^j_a \end{Bmatrix}_{r\times 1} \\ &= [\bar{\mathbf{D}}^j \mathbf{X}^j]_{n\times r} (\mathbf{p}^j)_{r\times 1} \end{aligned} \tag{36}$$

As the wave functions of unrestrained components are not constrained, there is a rigid body mode corresponding to the zero energy level in the solution of (13). While there are 3 rigid body modes for 2-D structural analysis, there is only one rigid body mode for each unrestrained component in the solution of the Schrödinger equation. Thus $\bar{\mathbf{D}}^j$ contains an additional column vector in (36) compared to $\bar{\mathbf{D}}^j$ in (31). Due to the existence of the rigid body mode, the attachment modes $\mathbf{X}^j$ in (36) are computed differently to exclude the influence of the rigid body mode which is already included in $\bar{\mathbf{D}}^j$. To obtain $\mathbf{X}^j$, the Hamiltonian matrix in (13) is first partitioned as

$$\boldsymbol{\Phi}^j = \begin{bmatrix} \boldsymbol{\Phi}^j_{ii} & \boldsymbol{\Phi}^j_{if} & \boldsymbol{\Phi}^j_{ir} \\ \boldsymbol{\Phi}^j_{fi} & \boldsymbol{\Phi}^j_{ff} & \boldsymbol{\Phi}^j_{fr} \\ \boldsymbol{\Phi}^j_{ri} & \boldsymbol{\Phi}^j_{rf} & \boldsymbol{\Phi}^j_{rr} \end{bmatrix}_{n\times n} \tag{37}$$

where i denotes the number of interior nodes, r denotes the number of rigid body coordinates ($r = 1$ for the 2-D Schrödinger equation) and $f = a - r$ denotes the number of interface coordinates excluding the rigid body coordinate. Note that the rigid body coordinate can be assigned on any boundary node of the component. Similar to the restrained component case, we apply an analogy to structural dynamics analysis, the attachment modes for the wave functions can be written as

$$\mathbf{X}^j = \mathbf{F}^j_{n\times n} \begin{bmatrix} \mathbf{0}^j_i \\ \mathbf{I}^j_a \end{bmatrix}_{n\times a} - (\bar{\mathbf{D}}^j)_{n\times k} (\mathbf{E}^j)^{-1}_{k\times k} (\bar{\mathbf{D}}^j)^T_{k\times n} \begin{bmatrix} \mathbf{0}^j_i \\ \mathbf{I}^j_a \end{bmatrix}_{n\times a} \tag{38}$$

where the first term on the right hand side is the wave function response to the unit excitation at the interface coordinates excluding the contribution of the rigid body mode, the second term is the wave function response contribution from the retained wave functions same as in (35). The effect of the rigid body mode is excluded from $\mathbf{X}^j$ through the matrix $\mathbf{F}^j$ which is obtained as

$$\mathbf{F}^j = (\mathbf{P}^j_r)^T \mathbf{F}^j_c \mathbf{P}^j_r \tag{39}$$

where $\mathbf{P}^j_r$ is the inertia-relief projection matrix defined by

$$\mathbf{P}^j_r = \mathbf{I} - \mathbf{M}^j (\mathbf{D}^j_R)_{n\times r} (\mathbf{D}^j_R)^T_{r\times n} \tag{40}$$

with $\mathbf{D}^j_R$ being the constant rigid body mode vector, and $\mathbf{F}^j_c$ is the constrained flexibility matrix given by

$$\mathbf{F}^j_c = \begin{bmatrix} \begin{bmatrix} \boldsymbol{\Phi}^j_{ii} & \boldsymbol{\Phi}^j_{if} \\ \boldsymbol{\Phi}^j_{fi} & \boldsymbol{\Phi}^j_{ff} \end{bmatrix}^{-1}_{(n-1)\times(n-1)} & \mathbf{0}_{(n-1)\times 1} \\ \mathbf{0}_{1\times(n-1)} & \mathbf{0}_{1\times 1} \end{bmatrix}_{n\times n} \tag{41}$$

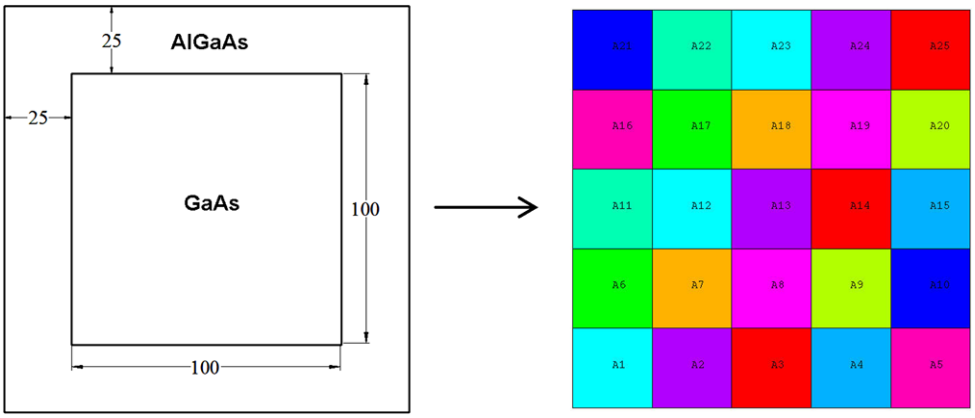

Fig. 2 *Left*: Quantum wire geometry (unit: Å). *Right*: Domain decomposition

Detailed derivation of $\mathbf{F}^j$, $\mathbf{P}_r^j$ and $\mathbf{F}_c^j$ can be found in [37]. For the sake of brevity, it is not repeated here.

To this end, the transformation matrix $\mathbf{T}^j$ of both restrained and unrestrained components are obtained. To simplify the coupling and assembly procedure, we can rewrite the transformation matrices given in (31), (36) in the same form as that in the fixed interface CMS approach given in (19) [38]. By using the lower part of (31) or (36), the generalized coordinate vector $\mathbf{p}_a^j$ can be expressed in terms of $\boldsymbol{\psi}_a^j$, and the result is applied back into the upper part of (31) or (36). As a result, (31), (36) can be rewritten in terms of the modal generalized coordinate vector $\mathbf{p}_i^j$ and the interface physical vector $\boldsymbol{\psi}_a^j$, which leads to

$$\begin{aligned}\boldsymbol{\psi}^j &= \begin{Bmatrix}\boldsymbol{\psi}_i^j \\ \boldsymbol{\psi}_a^j\end{Bmatrix}_{n\times 1} \\ &= \begin{bmatrix}\mathbf{D}_i^j - \mathbf{X}_i^j(\mathbf{X}_a^j)^{-1}\mathbf{D}_a^j & \mathbf{X}_i^j(\mathbf{X}_a^j)^{-1} \\ \mathbf{0}_a^j & \mathbf{I}_a^j\end{bmatrix}_{n\times r} \begin{Bmatrix}\mathbf{p}_i^j \\ \boldsymbol{\psi}_a^j\end{Bmatrix}_{r\times 1} \\ &= \check{\mathbf{T}}^j\check{\mathbf{z}}^j \end{aligned} \tag{42}$$

With the free interface component wave function approximation shown in (42) and the transformation matrix $\check{\mathbf{T}}^j$ computed, the component model reduction, assembly of the components and the recovery of the global wave functions are carried out by using the same procedure described in (22)–(30) which is not repeated here.

4 Results

4.1 Quantum wire

To demonstrate the validity and the efficiency of the CMS approaches for quantum mechanical electrostatic analysis of nanostructures and devices, in the first example, we consider a simple 2-D GaAs/AlGaAs quantum wire as shown in Fig. 2. The effective electron masses of GaAs and AlGaAs are set to be $m^*_{\text{GaAs}} = 0.0665m_0$ and $m^*_{\text{AlGaAs}} = 0.0858m_0$, respectively, where m_0 is the vacuum electron mass. The cross-sectional dimensions of the quantum wire are 150 Å × 150 Å for the outer boundary and 100 Å × 100 Å for the GaAs core. The heterojunction step potential between GaAs and AlGaAs is set to be 0.276 eV. The AlGaAs region is n-typed with a donor concentration of 10^{18} cm^{-3}. As electrons dominate, we ignore the hole concentration in our simulation. A homogeneous Dirichlet boundary condition is applied along the external boundary when solving the Schrödinger equation while a homogeneous Neumann boundary condition is used for Poisson equation. In the calculation by the CMS approaches, we decompose the entire domain into a set of components as shown in Fig. 2 (right). Both the fixed and free interface CMS approaches are applied to solve the Schrödinger equation with the same number of components to obtain the energy levels and corresponding wave functions in the structure.

Figures 3 and 4 shows the electron concentrations and potential profiles obtained from the two CMS approaches on a 120 × 120 mesh domain with 5 × 5 equal-size components (576 elements in each component). For each component, 5 component wave functions are retained in each component for the construction of the basis vectors in both approaches. In calculation of the electron concentration, 10 eigen-pairs computed by the Schrödinger equation are used, which proved to be sufficient to provide an accurate solution for the electron concentration. The results obtained from two CMS approaches are almost identical to the results obtained from the direct finite element solution (not shown).

To compare the computational cost of the two CMS approaches and direct method, the total number of elements within the domain is varied from 30 × 30 to 240 × 240 while the number of components is kept fixed, which is 25. Figure 5 shows CPU time comparison of those three approaches. It is shown that, for a coarse mesh, the CPU time of the direct FEM and the CMS approaches is similar.

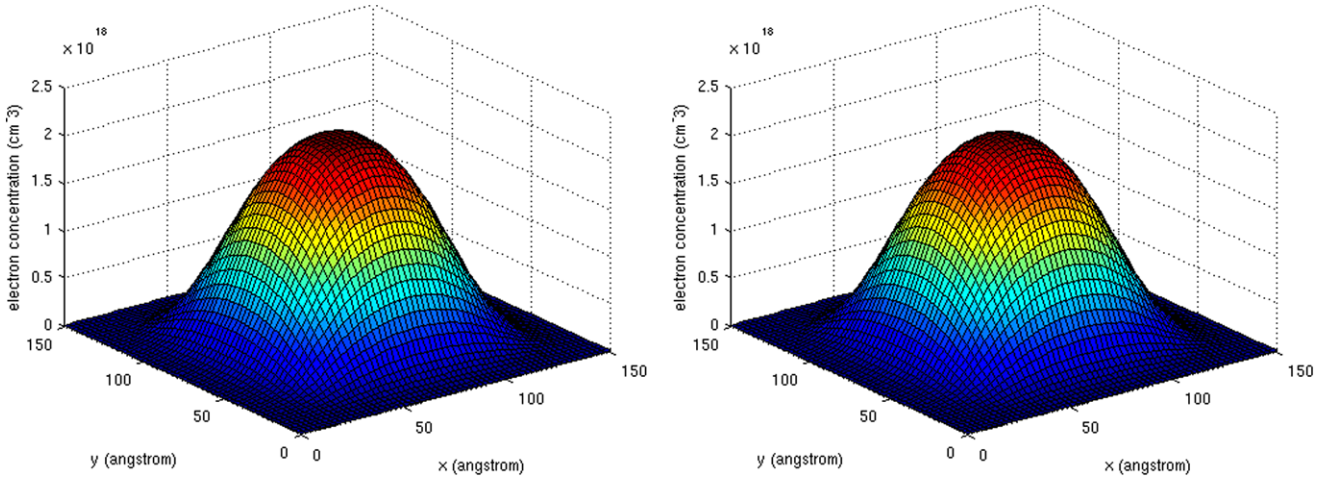

Fig. 3 Electron concentration computed using fixed (*left*) and free (*right*) interface CMS approaches

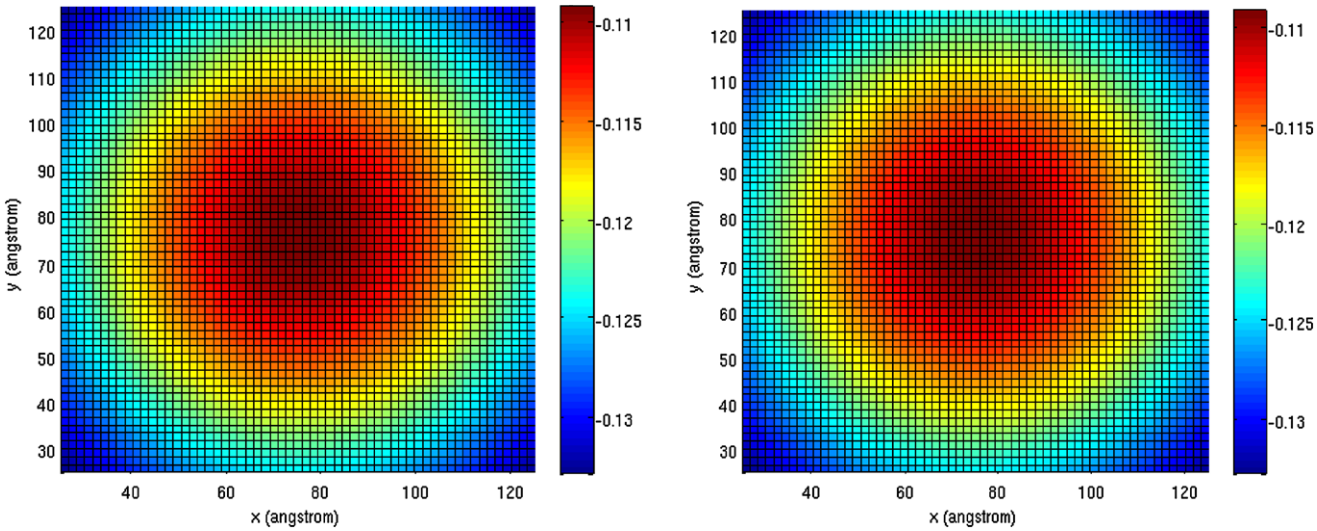

Fig. 4 Potential profile computed using fixed (*left*) and free (*right*) interface CMS approaches

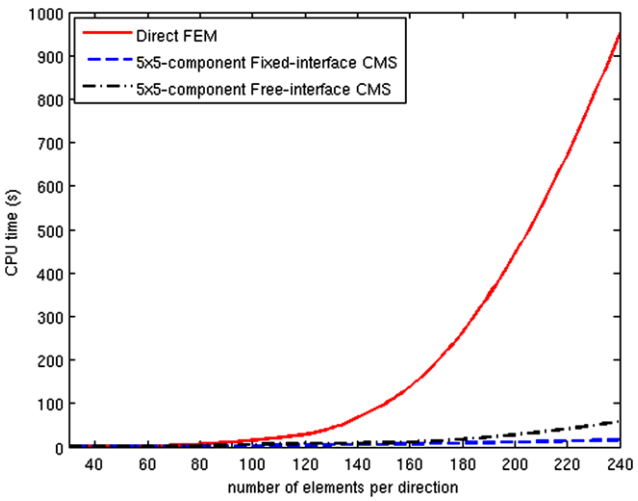

Fig. 5 CPU time comparison of the three methods

However, when the number of elements increases, the CMS approaches reduce the computational cost significantly. As shown in the figure, when the domain is meshed with 240 × 240 elements, the CPU time used by direct FEM is nearly 60 times and 17 times of those used by the fixed interface CMS approach and the free interface CMS approach, respectively. Between the CMS approaches, the free interface CMS is more expensive than the fixed interface CMS due to the extra matrix manipulations required in the method as described in Sect. 3.

To further investigate the accuracy of the CMS approaches, we vary the number of components as well as the number of retained component wave functions in each component. The error between the results computed with CMS and that computed with direct FEM is measured by using a global error measure with respect to the direct FEM

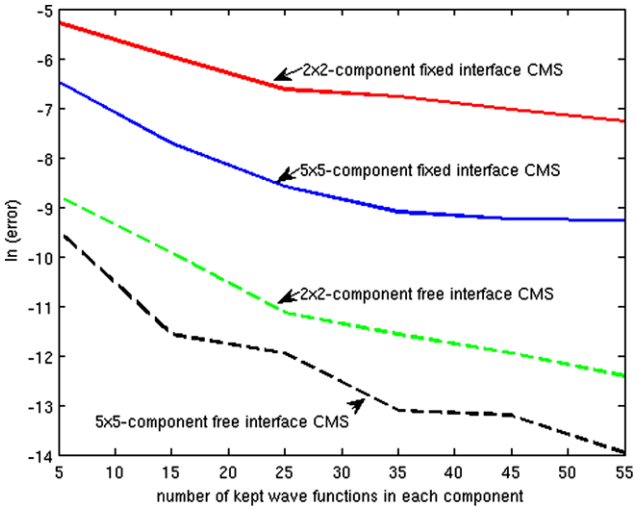

Fig. 6 Error in electron concentration for the fixed and free interface CMS approaches

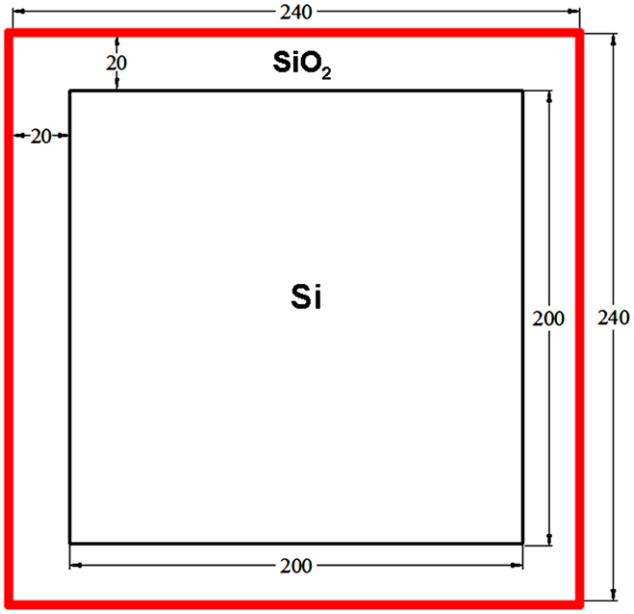

Fig. 7 GAA MOSFET transverse cross-section (unit: Å)

solution [41]

$$\varepsilon = \frac{1}{|\mu^{(e)}|}\sqrt{\frac{1}{NP}\sum_{I=1}^{I=NP}\left[\mu_I^{(e)} - \mu_I^{(c)}\right]^2} \tag{43}$$

where ε is the error in the solution and the superscripts (e) and (c) denote the direct FEM and CMS results, respectively, NP denotes the total DOFs.

Figure 6 shows the final electron concentration errors between the FEM and the CMS approaches as a function of the number of components and retained component wave functions. It is shown that the error decreases in both CMS approaches as the number of components and retained component wave functions increases. However, the error of the free interface CMS is significantly smaller than that of the fixed interface CMS. The convergence rate of the free interface CMS is consistently larger than that of the fixed interface CMS. To achieve the same accuracy, the free interface CMS requires much less retained component wave functions in each component as shown in the figure.

4.2 Gate-All-Around (GAA) MOSFET

In the second example, we simulate a GAA MOSFET and compute the electron concentration and potential profile in the cross section perpendicular to the transport direction within the device. The cross section of GAA MOSFET is depicted in Fig. 7. The size of the device is 240 Å × 240 Å. The central part of the MOSFET is intrinsic Si with a dimension of 200 Å × 200 Å. The thickness of the surrounding SiO_2 layer is 20 Å. The metal gate work function is assumed to be 4.05 eV. A voltage of 0.5 V is applied on the gates. The effective mass of SiO_2 is $m^*_{SiO_2} = 0.5m_0$. The conduction band of Si has six equivalent valleys, with three different pairs of conduction band minima. The transverse and longitudinal electron masses are defined as $m_t^* = 0.19m_0$ and $m_l^* = 0.91m_0$, respectively. The Schrödinger equation is solved three times for each pair of the conduction band minima. Then three different sets of eigen-pairs can be obtained. The heterojunction step potential between silicon substrate and the oxide is 3.34 eV. The relative dielectric constants for the silicon substrate and oxide are set to be $\epsilon_{Si} = 11.7$ and $\epsilon_{SiO_2} = 3.9$, respectively. The first 30 eigen-pairs are used to obtain an accurate description of electron concentration within the device.

Figures 8 and 9 show the electron concentration and electrostatic potential obtained with the fixed and free interface CMS approaches, respectively. In both simulations, 16 components of the same size and 5 retained component wave functions in each component are used. The mesh size is 96×96. It is observed that the results obtained by both CMS approaches are consistent with the results obtained by the direct FEM (not shown).

The CPU time for the GAA MOSFET simulations by using the direct FEM, the fixed and free interface CMS approaches with 5 retained component wave functions per component is compared in Fig. 10. In the computation, the whole domain is decomposed into 16 equal-sized components. The mesh size is ranging from 48×48 to 192×192. It is shown that with more elements (finer mesh), the computational cost reduction through the CMS approaches becomes more significant. In this example, when the domain is meshed with 192×192 elements, the fixed and free interface CMS approaches are about 28 times and 11 times faster than the direct approach, respectively.

By using the error measure given in (43), the electron concentration error of the CMS approaches as a function of

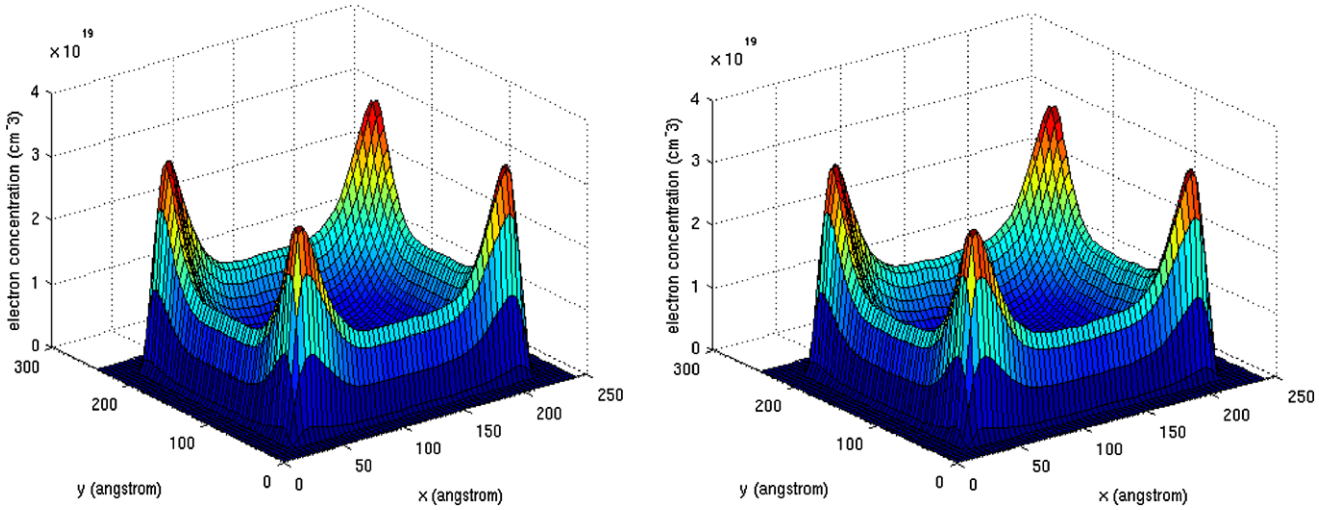

Fig. 8 Electron concentration computed using fixed (*left*) and free (*right*) interface CMS approaches

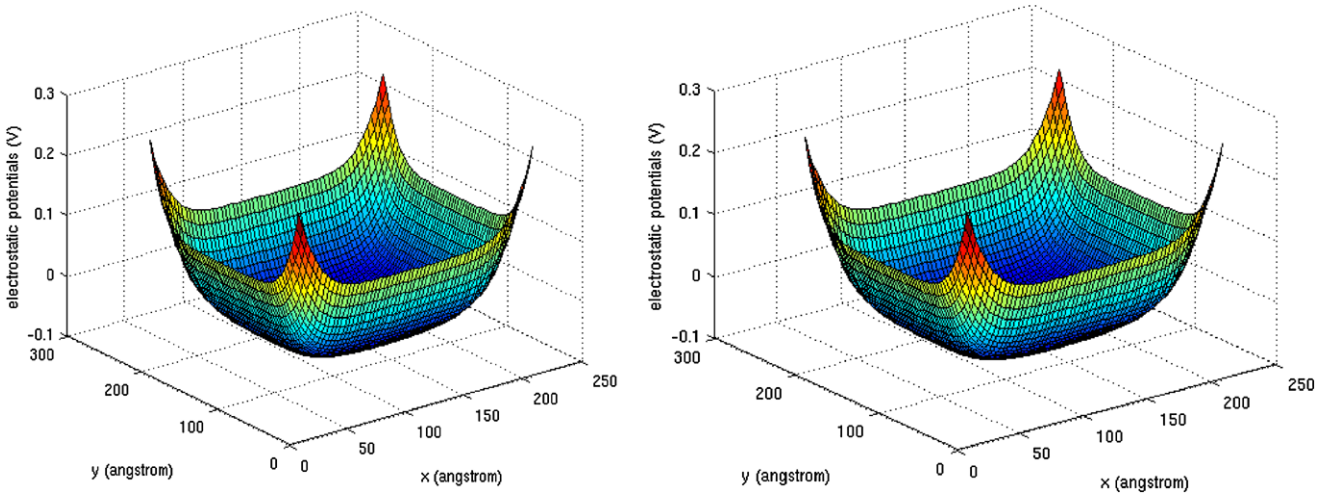

Fig. 9 Electrostatic potential computed using fixed (*left*) and free (*right*) interface CMS approaches

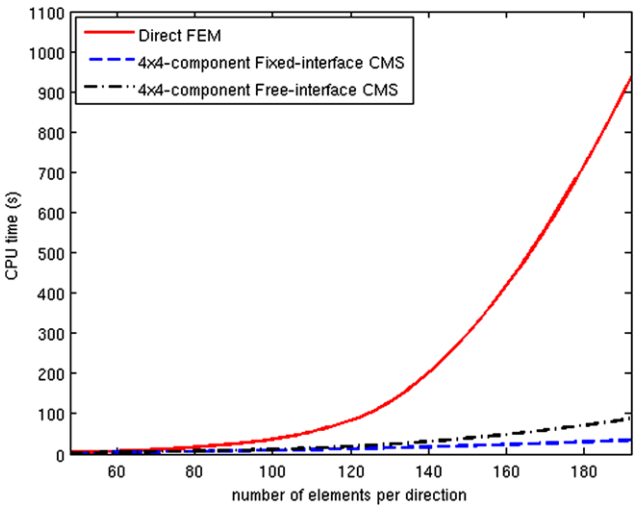

Fig. 10 CPU time comparison of the three methods

the number of components and retained component wave functions in each component is calculated and shown in Fig. 11. The convergence behavior is similar to that shown in Fig. 6. While the result improves as the number of retained component wave functions increases, error of the free interface CMS is significantly lower compared to the fixed interface CMS.

As shown in the first two examples, with the same number of component wave functions kept in each component, the results obtained with the free interface CMS approach are more accurate than those by the fixed interface CMS approach. To investigate the reasons, the eigenvalues computed by both methods are compared with those obtained by direct approach. Figure 12 shows the relative error of eigenvalues of the CMS solutions compared to the direct solution. The results are obtained by keeping 10 wave functions in each component, and the first 30 eigen-pairs are calculated. It is

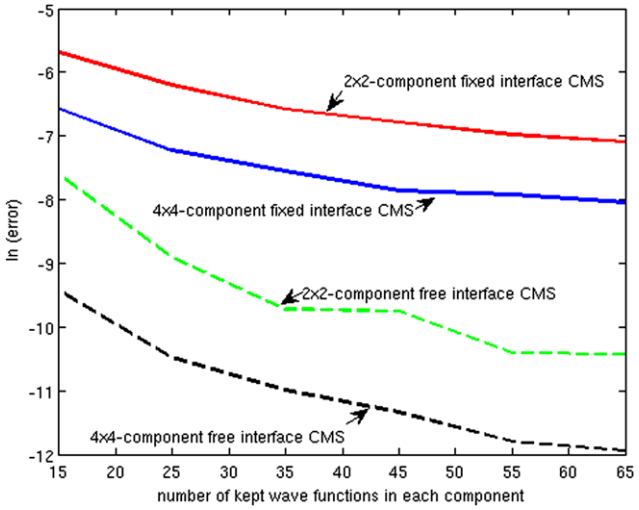

Fig. 11 Error in electron concentration for the fixed and free interface CMS approaches

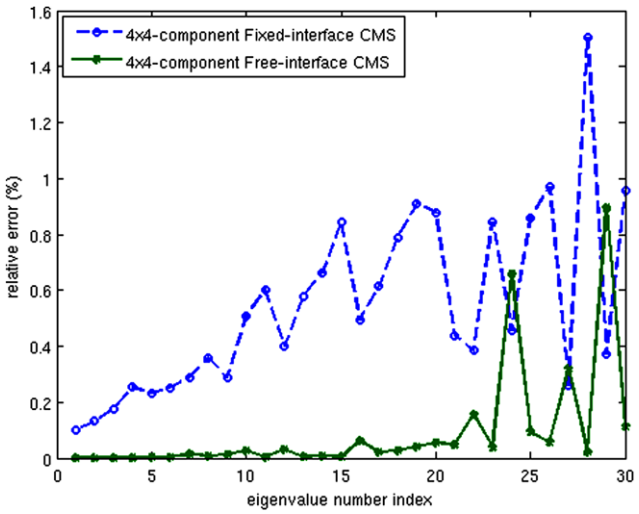

Fig. 12 Error of computed eigenvalues from both CMS approaches

shown that the relative error introduced by the free interface CMS approach is much smaller than that from the fixed interface CMS approach. Since the accuracy of the electron concentration obtained in every Schrödinger-Poisson iteration directly depends on the accuracy of the calculated eigen-pairs, the free interface CMS can therefore offer more accurate final results of electron concentration and potential.

4.3 Trigate MOSFET with rounded corners

In the third example, we simulate a trigate MOSFET with rounded corners as shown in Fig. 13. The dimensions of the device are shown in the figure. The central part of the MOSFET is intrinsic Si. The remaining part is the SiO_2 layer. All the parameters for the Si and SiO_2 are the same as given in the second example. In this case, the gates are attached to the boundary of the device above $y = 20$ Å (depicted by the red line in Fig. 13). A voltage of 0.5 V is applied on the gates. In the CMS calculations, the domain is decomposed into 39 components (shown in Fig. 13). To correctly describe the electron concentration in the cross-section perpendicular to the carrier transport direction, 40 eigen-pairs are retained in computing the electron concentration using (6). In this example, the performance of two CMS approaches is similar to that in the second example. The electron concentration and electrostatic potential obtained with both CMS approaches match the results by the direct approach well. Figures 14 and 15 show the final results obtained by both CMS approaches with a mesh of 15600 elements. In the calculation, five component wave functions are retained in each component to solve for the 40 eigen-pairs that are used to compute the electron concentration.

The CPU time comparison for the MOSFET simulations is shown in Fig. 16. The CPU time for the trigate MOSFET simulations by using the direct approach, the fixed and free interface CMS approaches with 5 retained wave functions per component is compared. It is shown that for the fine mesh with 47775 elements in total, the fixed and free interface CMS approaches are about 13 times and 7 times faster than the direct FEM, respectively.

The error comparison for the CMS approaches is shown in Fig. 17. Once again, the free interface CMS approach shows a superior performance in the solution accuracy as well as the convergence rate.

5 Conclusion

In this paper, two component mode synthesis (CMS) approaches, namely, the fixed interface CMS approach and the free interface CMS approach, are presented and compared for 2-D quantum mechanical electrostatic analysis of nanoscale structures and devices with arbitrary geometries. The CMS approaches are employed to compute the charge concentrations and potential profiles of several nanoscale structures and devices, including a quantum wire, a GAA MOSFET and a trigate MOSFET. The results obtained from the CMS approaches are compared with those obtained from the direct FEM. It is shown that both CMS approaches can yield accurate results with much less computational cost compared to the direct finite element analysis. To achieve the same accuracy, the number of component wave functions required to be retained in the free interface CMS approach is much less than that in the fixed interface CMS approach. The reduction of computational cost becomes more significant as the total degrees of freedom of the system increase. In general, the fixed interface CMS approach is more efficient than the free interface CMS approach due to its simpler matrix operations in the computational process.

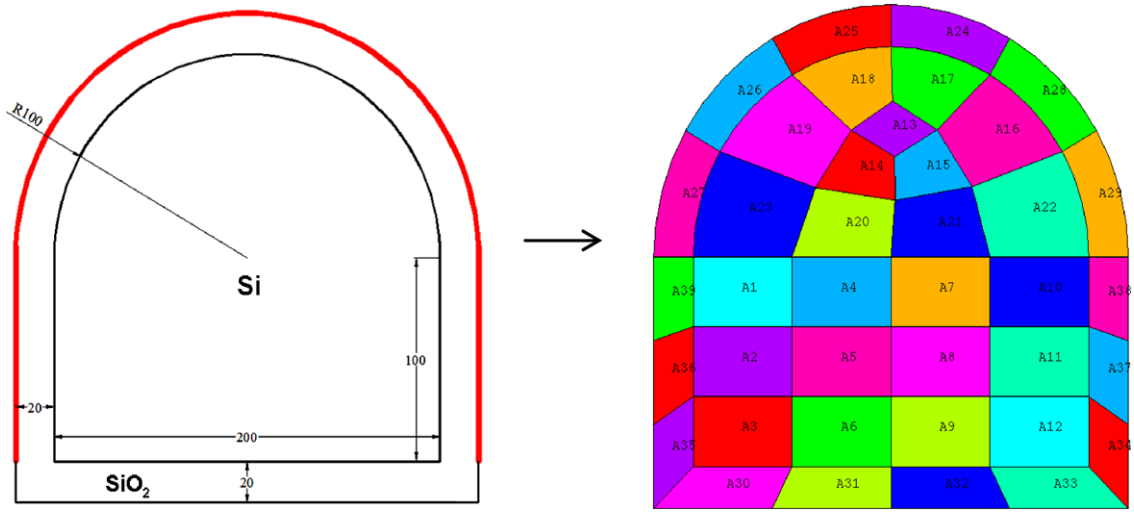

Fig. 13 Trigate MOSFET cross-section with rounded corners (unit: Å) and its substructuring result

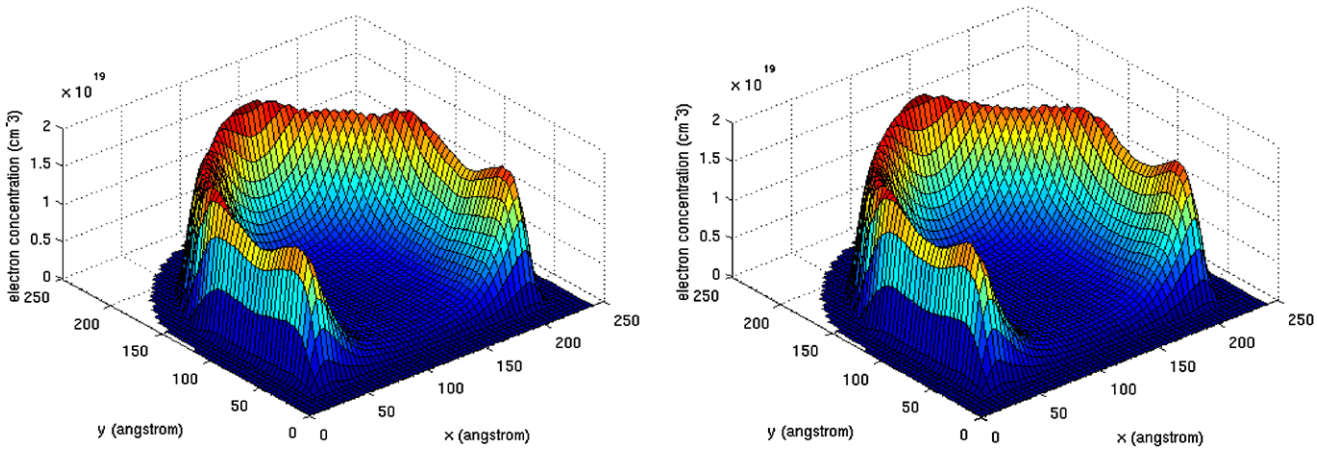

Fig. 14 Electron concentration computed using fixed (*left*) and free (*right*) interface CMS approaches

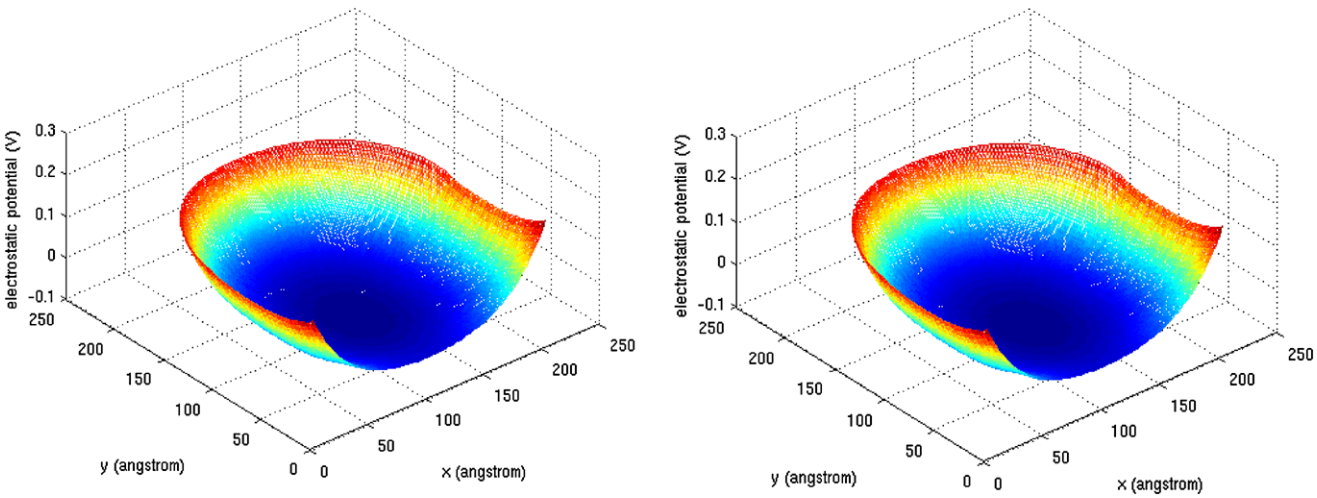

Fig. 15 Electrostatic potential computed using fixed (*left*) and free (*right*) interface CMS approaches

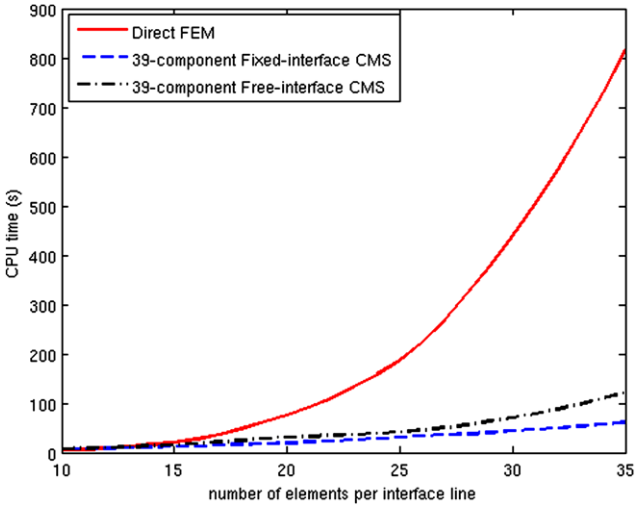

Fig. 16 CPU time comparison of the three methods

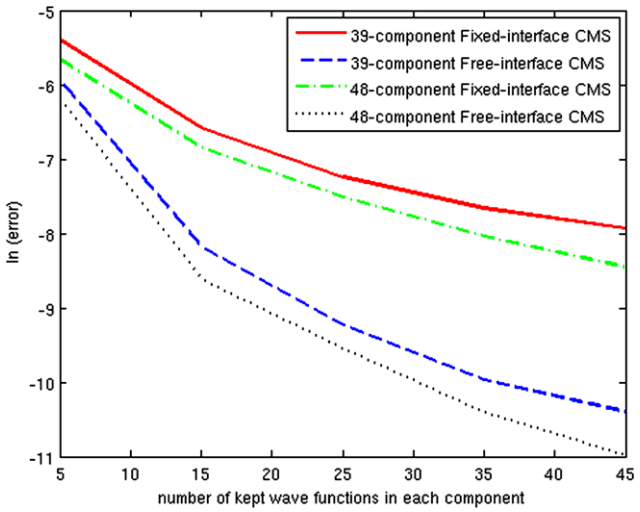

Fig. 17 Error in electron concentration for the fixed and free interface CMS approaches

Acknowledgements We gratefully acknowledge support by the National Science Foundation under Grant CMMI-0800474.

References

1. Wong, H., Frank, D.J., Solomon, P.M.: Device design considerations for double gate, ground plane, and single-gated ultra-thin SOI MOSFET's at the 25 nm channel length generation. IEDM Tech. Dig., pp. 407-410 (1998)
2. Omura, Y., Kurihara, K., Takahashi, Y., Ishiyanma, T., Nakajima, Y., Izumi, K.: 50-nm channel nMOSFET/SIMOX with an ultra-thin 2- or 6-nm thick silicon layer and their significant features of operations. IEEE Electron Device Lett. **18**(5), 190–193 (1997)
3. Park, J., Colinge, J.: Multiple-gate SOI MOSFETs: device design guidelines. IEEE Trans. Electron Devices **49**(12), 2222–2229 (2002)
4. Hason, S., Wang, J., Lundstrom, M.: Device design and manufacturing issues for 10 nm-scale MOSFETs: a computational study. Solid-State Electron. **48**, 867–875 (2004)
5. Lopez-Villanueva, J.A., Melchor, I., Gamiz, F., Banqueri, J., Jimenez-Tejada, J.A.: A model for the quantized accumulation layer in metal-insulator-semiconductor structures. Solid-State Electron. **38**(1), 203–210 (1995)
6. Ohkura, Y.: Quantum effects in Si n-MOS inversion layer at high substrate concentration. Solid-State Electron. **33**(12), 1581–1585 (1990)
7. Janik, T., Majkusiak, B.: Analysis of the MOS transistor based on the self-consistent solution to the Schrödinger and Poisson equations and on the local mobility model. IEEE Trans. Electron Devices **45**(6), 1263–1271 (1998)
8. Tang, Z., Xu, Y., Li, G., Aluru, N.R.: Physical models for coupled electromechanical analysis of silicon nanoelectromechanical systems. J. Appl. Phys. **97**(11), 114304 (2005)
9. Ravaioli, U., Winstead, B., Wordelman, C., Kepkep, A.: Monte Carlo simulation for ultra-small MOS devices. Superlattices Microstruct. **27**(3), 137–145 (2000)
10. Dattta, S.: Nanoscale device modeling: the Green's function method. Superlattices Microstruct. **28**(4), 253–278 (2000)
11. Ren, Z., Venugopal, R., Goasguen, S., Datta, S., Lundstrom, M.S.: nanoMOS 2.5: a two-dimensional simulator for quantum transport in double-gate MOSFETs. IEEE Trans. Electron Devices **50**(9), 1914–1925 (2003)
12. Xu, Y., Aluru, N.R.: Multiscale electrostatic analysis of silicon nanoelectromechanical systems (NEMS) via heterogeneous quantum models. Phys. Rev. B **77**(7), 075313 (2008)
13. Stern, F.: Self-consistent results for n-type Si inversion layers. Phys. Rev. B **5**(12), 4891–4899 (1972)
14. Khan, H., Mamaluy, D., Vasileska, D.: Fully 3D self-consistent quantum transport simulation of double-gate and tri-gate 10 nm FinFETs. J. Comput. Electron. **7**, 346–349 (2008)
15. Li, G., Aluru, N.R.: Hybrid techniques for electrostatic analysis of nanoelectromechanical systems. J. Appl. Phys. **96**(4), 2221–2231 (2004)
16. Sune, J., Olivo, P., Ricco, B.: Self-consistent solution of the Poisson and Schrödinger in accumulated semiconductor-insulator interfaces. J. Appl. Phys. **70**(1), 337–345 (1991)
17. Tan, I.-H., Snider, G.L., Chang, L.D., Hu, E.L.: A self-consistent solution of Schrödinger-Poisson equations using a nonuniform mesh. J. Appl. Phys. **68**(8), 4071–4076 (1990)
18. Kerkhoven, T., Galick, A.T., Ravaioli, U., Arends, J.H., Saad, Y.: Efficient numerical simulation of electron states in quantum wires. J. Appl. Phys. **68**(7), 3461–3469 (1990)
19. Trellakis, A., Galick, A.T., Pacelli, A., Ravaioli, U.: Iteration scheme for the solution of the two-dimensional Schrödinger-Poisson equations in quantum structures. J. Appl. Phys. **81**(12), 7880–7884 (1997)
20. Trellakis, A., Ravaioli, U.: Computational issues in the simulation of semiconductor quantum wires. Comput. Methods Appl. Mech. Eng. **181**, 437–449 (2000)
21. Godoy, A., Ruiz-Gallardo, A., Sampedro, C., Gamiz, F.: Quantum-mechanical effects in multiple-gate MOSFETs. J. Comput. Electron. **6**, 145–148 (2007)
22. Garcia Ruiz, F.J., Godoy, A., Gamiz, F., Samperdro, C., Donetti, L.: A comprehensive study of the corner effects in pi-gate MOSFETs including quantum effects. IEEE Trans. Electron Devices **54**(12), 3369–3377 (2007)
23. Colinge, J.P.: Quantum-wire effects in trigate SOI MOSFETs. Solid-State Electron. **51**, 1153–1160 (2007)
24. Garcia Ruiz, F.J., Tienda-Luna, I.M., Godoy, A., Donetti, L., Gamiz, F.: Equivalent oxide thickness of trigate SOI MOSFETs with high-k insulators. IEEE Trans. Electron Devices **56**(11), 2711–2719 (2009)

25. Tang, X., Baie, X., Colinge, J.P., Gustin, C., Bayot, V.: Two-dimensional self-consistent simulation of a triangular P-channel SOI nano-flash memory device. IEEE Trans. Electron Devices **49**(8), 1420–1426 (2002)
26. Colinge, J.P., Alderman, J.C., Xiong, W., Cleavelin, C.R.: Quantum-mechanical effects in trigate SOI MOSFETs. IEEE Trans. Electron Devices **53**(5), 1131–1135 (2006)
27. Wang, J., Polizzi, E., Lundstrom, M.: A three dimensional quantum simulation of silicon nanowire transistors with the effective-mass approximation. J. Appl. Phys. **96**(4), 2192 (2004)
28. Shin, M.: Three-dimensional quantum simulation of multigate nanowire field effect transistors. Math. Comput. Simul. **79**, 1060–1070 (2008)
29. Craig, R., Bampton, M.: Coupling of substructures for dynamic analysis. AIAA J. **6**, 1313 (1968)
30. Min, K.-W., Igusa, T., Achenbach, J.D.: Frequency window method for forced vibration of structures with connected substructures. J. Acoust. Soc. Am. **92**(5), 2726–2733 (1992)
31. Shyu, W.H., Gu, J., Hulbert, G.M., Ma, Z.D.: On the use of multiple quasi-static mode compensation sets for component mode synthesis of complex structures. Finite Elem. Anal. Des. **35**, 119–140 (2000)
32. Shyu, W.H., Ma, Z.D., Hulbert, G.M.: A new component mode synthesis method: quasi-static mode compensation. Finite Elem. Anal. Des. **24**, 271–281 (1997)
33. Markovic, D., Park, K.C., Ibrahimbegovic, A.: Reduction of substructural interface degrees of freedom in flexibility-based component mode synthesis. Int. J. Numer. Methods Eng. **70**, 163–180 (2007)
34. Craig, R.R., Chang, C.J.: Free-interface methods of substructure coupling for dynamic analysis. AIAA J. **14**(11), 1633–1635 (1976)
35. Tournour, M.A., Atalla, N., Chiello, O., Sgard, F.: Validation, performance, convergence and application of free interface component mode synthesis. Comput. Struct. **79**, 1861–1876 (2001)
36. Koutsovasilis, P., Beitelschmidt, M.: Model order reduction of finite element models: improved component mode synthesis. Math. Comput. Model. Dyn. Syst. **16**(1), 57–73 (2010)
37. Craig, R.R., Kurdila, A.J.: Fundamentals of Structural Dynamics. Wiley, New York (2006)
38. Craig, R.R.: Coupling of substructures for dynamic analysis: an overview. In: Structures, Structural Dynamics and Material Conference (2000). AIAA-2000-1573
39. Rixen, D.J.: A dual Craig-Bampton method for dynamic substructuring. J. Comput. Appl. Math. **168**, 383–391 (2004)
40. Li, G.: A multilevel component mode synthesis approach for the calculation of the phonon density of states of nanocomposite structures. Comput. Mech. **42**(4), 593–606 (2008)
41. Aluru, N., Li, G.: Finite cloud method: a true meshless technique based on a fixed reproducing kernel approximation. Int. J. Numer. Methods Eng. **50**(10), 2373–2410 (2001)